High Performance Magnetic Mass-Enhanced Triboelectric-Electromagnetic Hybrid Vibration Energy Harvester Enabling Totally Self-Powered Long-Distance Wireless Sensing

Ziyue Xi, Hongyong Yu, Hengxu Du, Hengyi Yang, Yawei Wang, Mengyuan Guan, Zhaoyang Wang, Hao Wang, Taili Du,* and Minyi Xu*

Wireless sensor networks play a significant role in various fields, and it is promising to construct a totally self-powered wireless sensor network by harvesting unused mechanical vibration energy. Here, a magnetic mass-enhanced triboelectric-electromagnetic hybrid nanogenerator (MM-HNG) is proposed for harvesting mechanical vibration energy. The additional magnets generate magnetic fields for electromagnetic power generation. As an additional mass effectively increases the membrane's amplitude, thereby enhancing the output performance of the MM-HNG. The peak power density of TENG in the MM-HNG reaches 380.4 W m^{-3}, while the peak power density of EMG achieves 736 W m^{-3}, which can charge a 0.1 F capacitor rapidly. In addition, a totally self-powered wireless sensing system is constructed, with the integrated microcontroller unit (MCU), which detects and processes various sensing parameters and controls wireless transmission. The system features rapid transmission speeds and an extensive transmission range (up to 1 km), and its effectiveness has been validated in a practical application aboard an actual ship. The results illustrate the MM-HNG's broad applicability across various Internet of Things (IoT) scenarios, including smart machinery, smart transportation, and smart factories.

1. Introduction

With the development of IoT and big data technology,[1] smart wireless sensor networks have gained widespread use and attention in various sectors,[2] such as smart ships,[3] smart factories,[4]

Z. Xi, H. Yu, H. Du, H. Yang, M. Guan, Z. Wang, H. Wang, T. Du, M. Xu
Dalian Key Lab of Marine Micro/Nano Energy and Self-powered Systems
Marine Engineering College
State Key Laboratory of Maritime Technology and Safety
Dalian Maritime University
Dalian 116026, China
E-mail: dutaili@dlmu.edu.cn; xuminyi@dlmu.edu.cn
Y. Wang
Internet of Things Thrust
The Hong Kong University of Science and Technology (Guangzhou)
Nansha, Guangzhou, Guangdong 511400, China

and so on. It can realize real-time monitoring and data collection in a wide range of areas. However, the power supply for these wireless sensing devices encounters challenges, including limited battery capacity, complex cable distribution, and restricted transmission distance. These factors collectively restrict the widespread distribution and sustained, stable, and efficient operation of wireless sensor networks.[5–7]

Therefore, it becomes crucial to explore sustainable energy solutions. There is a large amount of energy in the environment that has not been used, such as wind energy,[8] wave energy,[9] acoustic energy,[10] thermal energy,[11] vibration energy,[12] etc. Among these energy sources, vibration energy is the most widely distributed, ubiquitous, and consistently stable. Therefore, harvesting this unutilized vibration energy provides an effective means to address the power challenges faced by wireless sensor nodes. The triboelectric nanogenerator (TENG) as a new type of generator is proposed by Yu et al.,[13] which is a novel type of generator characterized by high output voltage, low cost, a simple and easy-to-fabricate structure, and high adaptability.[14] Research has demonstrated that TENG can serve as an energy harvesting device and function as various active sensors, such as wind speed sensor,[15] flow velocity sensor,[16] underwater whisker sensor,[17] acoustic sensor,[18] vibration sensor,[19] and some microsensors.[20–22] However, the TENG is still limited by its own low current and high internal resistance, and there are still challenges in using the TENG alone to achieve total self-power for wireless sensing and transmission systems.

At present, a large number of researchers have employed various techniques to harvest vibration energy, including electromagnetic,[23] piezoelectric,[24] triboelectric,[14] and hybrid with this. Hybridization of triboelectric with other energy harvesting methods, such as electromagnetic,[25] piezoelectric,[26] and photovoltaic,[27] has become an effective way to improve the energy harvesting capability of the system. Among them,

**ADVANCED
SCIENCE NEWS**

www.advancedsciencenews.com

**ADVANCED
MATERIALS
TECHNOLOGIES**

www.advmattechnol.de

combining the high voltage output of TENG with the high current capabilities of the electromagnetic generator (EMG) has emerged as an optimal approach to enhance energy harvesting efficiency. Fan et al.[28] proposed that the power output performance of EMG and TENG exhibit a unique complementary relationship, where coupling them enhances the overall power output. Utilizing hybrid triboelectric-electromagnetic nanogenerators for environmental energy harvesting has proven to be a remarkably effective method for capturing energy such as wind,[29–32] waves,[33–36] and vibration.[37–44] Quan et al.[25] initially proposed a hybrid triboelectric-electromagnetic nanogenerator for vibration energy harvesting, which significantly improved power generation performance. To further enhance the power generation capabilities of the generator and meet the electrical power requirements of a totally self-powered long-distance wireless sensing system, more and more researchers are now investigating triboelectric-electromagnetic hybrid nanogenerators. To satisfy the demands of wireless sensing nodes, a variety of self-powered wireless sensor systems have been developed by researchers using triboelectric-electromagnetic hybrid nanogenerators, representative of which include Gao et al.[42] and Shen et al.[43] Although they use Bluetooth or WIFI function to realize part of the information transmission, these systems require further enhancement to adequately address the multi-information and long-distance transmission needs of wireless sensor networks. Consequently, further research is necessary to develop a totally self-powered long-distance wireless sensing system.

In this work, to solve the above problem, a novel magnetic mass-enhanced triboelectric-electromagnetic hybrid nanogenerator (MM-HNG) is designed and proposed. The MM-HNG efficiently harvests vibration energy from mechanical equipment by integrating the TENG and EMG. The maximum power of TENG in MM-HNG reaches 2.14 mW, with a maximum power density of 380.4 W m^{-3}, while the maximum capacity of EMG achieves 41.04 mW, with a maximum power density of 736 W m^{-3}, which can quickly recharge a 0.1 F supercapacitor. Even more, the TENG in MM-HNG can also serve as a vibration frequency sensor across a broad frequency range. In addition, a totally self-powered long-distance wireless sensing system by the MM-HNG is constructed, which is capable of real-time wireless transmission of temperature, humidity, and equipment vibration frequency information over distances exceeding 1 kilometer. At last, the MM-HNG has been successfully demonstrated to achieve wireless transmission from the generator engine to the engine control room in a real ship engine room by harvesting the actual vibration energy of the generator engine. Therefore, the MM-HNG in this work introduces a new approach for constructing a totally self-powered distributed wireless sensing system. This also demonstrates that the MM-HNG has a broad spectrum of application scenarios within the Internet of Things domain.

2. Results and Discussion

2.1. Structure and Working Principle of the MM-HNG

2.1.1. Application Scenario and Structure Schematic of MM-HNG

Figure 1a vividly illustrates the scenario diagram of the total self-powering of the remote wireless sensor system, made possible by the vibration energy harvesting capabilities of the MM-HNG. Its simple structure and excellent performance enable it to harvest vibration energy from a wide range of mechanical devices and pipelines. The MM-HNG combines a triboelectric nanogenerator with an electromagnetic generator to efficiently harvest vibration energy from the environment. Additionally, it serves as a frequency monitoring sensor. This capability of harvesting vibration energy enables the MM-HNG to support totally self-powered wireless transmission over long distances, reaching up to 1 km. The MM-HNG is composed of several key components: a magnet that generates a magnetic field and serves as an additional mass; an FEP coated with conductive ink and conductive fabric, functioning as a mover; and a stator that includes a PLA frame and coils, as shown in Figure 1a. When the vibration is generated, the magnet acts as an additional mass, pushing the FEP away from the conductive fabric and creating a moving magnetic field that induces current in the coil. The FEP membrane, an excellent electronegative electret material, retains charge on its surface, while the conductive fabric, a positive triboelectric material, generates electricity through contact and separation. The MM-HNG physical diagram is shown in Figure S1 (Supporting Information).
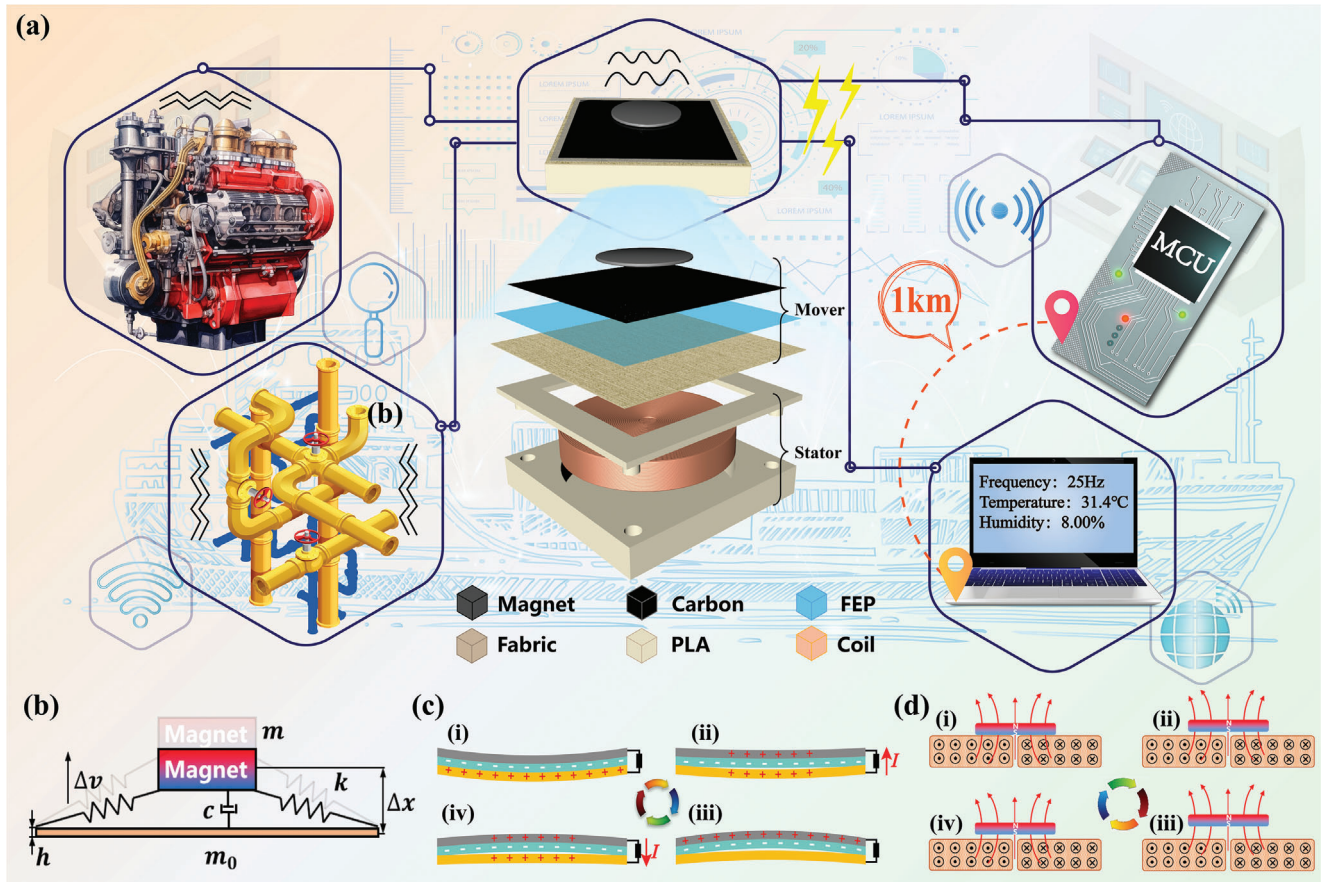
2.1.2. The Dynamics of MM-HNG

Figure 1b also shows a physical model of the membrane vibration, where the membrane can be considered as a spring-like structure. The addition of magnets increases the inertia of the membrane's motion, thereby enhancing its amplitude. This results increase the amplitude of the membrane, resulting in a better contact separation motion between the FEP membrane and the conductive fabrics, ultimately improving the triboelectric power generation. To investigate the motion characteristics of MM-HNG, a set of vibration energy test platforms is constructed as shown in Figure S2 (Supporting Information). The vibration source is a shaker with adjustable vibration signals controlled by a signal generator and a power amplifier. The vibration acceleration and amplitude of the MM-HNG are measured with an acceleration sensor and a displacement sensor, respectively. Additionally, a high-speed camera is utilized to observe the membrane's vibration state. The excitation of the shaker is based on sinusoidal excitation, and its vibration dynamic equation is given by:

$$y = A \sin (\omega t + \varphi) \qquad (1)$$

$$a = A \omega^2 = A (2\pi f_0)^2 \qquad (2)$$

where y is the sine function of vibration excitation, A is the amplitude, ω is the angular frequency of vibration, a is the vibration acceleration of the shaker, and f_0 is the vibration frequency of the shaker. Therefore, according to the theory of additional mass thin film vibration and considering the additional damping and nonlinear effects when the thin film system is subjected to electromagnetic and frictional forces. the dynamic response equation of MM-HNG under vibrational excitation is expressed as:

$$f = \frac{1}{2\pi} \sqrt{\frac{T}{\mu} + \frac{m}{\mu + \iint m (x, y) \, dA} - \zeta} \qquad (3)$$

**ADVANCED
SCIENCE NEWS**

www.advancedsciencenews.com

**ADVANCED
MATERIALS
TECHNOLOGIES**

www.advmattechnol.de

Figure 1. Design and principle of MM-HNG self-powered wireless signal monitoring system. a) Application scenario and structure schematic of MM-HNG. b) Dynamic model of MM-HNG vibration. c) Working principle of TENG. d) Working principle of EMG.

$$A = C e^{-\zeta t} \sqrt{E h f^2 \rho} \qquad (4)$$

where f is the free vibration frequency of the membrane, T is the tension of the membrane, μ is the linear density of the membrane, m is the additional mass, and $\iint m(x, y) dA$ is the integral of the distribution function of the additional mass. ζ represents the total damping due to electromagnetism and friction, which reduces the natural frequency of the system. A is the amplitude, C is a constant, E is the elastic modulus of the membrane, h is the thickness of the membrane, and ρ is the density of the membrane. $e^{-\zeta t}$ is used to characterize the amplitude that decays with time, where t represents time. It can be seen that the amplitude of the membrane vibration has a close relationship with the additional magnet mass, and at the same time, the process of membrane vibration adheres to the principle of energy conservation, as described by the equation:

$$\int [F(t) v(t)] dt = \frac{1}{2} (m + m_0)(\Delta v)^2 + \frac{1}{2} k (\Delta x)^2 - c(\Delta v)^2 + \Delta E \quad (5)$$

where $F(t)$ is the external excitation given by the shaker, m_0 is the mass of the membrane, Δv is the change in vibration velocity, k is the elasticity coefficient of the membrane, c is the damping coefficient, ΔE is the energy of the electromagnetic field. Differences in the attached magnets affect the amplitude and magnetic

field strength of the MM-HNG, which in turn affects the output performance of the MM-HNG.

2.1.3. The working principle of the MM-HNG

The working principle of the TENG is illustrated in Figure 1c. As a contact-separated TENG, it generates electrical energy based on the principles of triboelectrification and electrostatic induction. In the initial state, as shown in Figure 1bi, the FEP membrane is in complete contact with the conductive fabric by the gravity of the magnet. This contact and subsequent separation lead to multiple interactions, causing the surface of the FEP membrane and the conductive fabric, which differ in electronegativity, to generate equal amounts of positive and negative charges, respectively. In the second stage, as depicted in Figure 1cii, the FEP membrane and magnet move upward, creating a separation from the conductive fabric. During this process, electrons transfer from the conductive ink electrode to the conductive fabric through an external circuit to equalize the potential difference between the FEP membrane and the conductive fabric. When the FEP membrane rises to its maximum height, the electric field reaches a new equilibrium, and the charge transfer stops (Figure 1ciii). Then, as the FEP membrane moves downward, the electron transfer reverses (Figure 1cvi). Finally, the FEP

ADVANCED
SCIENCE NEWS

www.advancedsciencenews.com

ADVANCED
MATERIALS
TECHNOLOGIES

www.advmattechnol.de

membrane and the conductive fabric come into contact again, returning the charge distribution to its initial state (Figure 1ci). Consequently, this process generates an alternating current. According to the operating principle of the contact-separated TENG, the open-circuit voltage is represented as:

$$V_{OC}^{TENG} = \frac{\sigma \Delta x}{\varepsilon_0} \tag{6}$$

where V_{OC}^{TENG} is the open circuit voltage of TENG, σ is the friction charge density, Δx is the relative displacement change of the membrane vibration, and ε_0 is the dielectric constant in a vacuum. To better demonstrate the potential change of TENG, finite element analysis is performed utilizing COMSOL to simulate the potential distribution between the two triboelectric layers, as depicted in Figure S3a (Supporting Information). The simulation results are in agreement with the experimental results.

The working principle of the EMG is illustrated in Figure 1d. Acting as both the magnetic field generator and additional mass, the magnet causes the FEP membrane to reciprocate vertically, resulting in changes in the magnetic field. According to Lenz's law, this motion induces a current in the conductor as it moves through the magnetic field. In the initial state, the magnet is in contact with the coil due to its gravity (Figure 1di). As the magnet vibrates, the magnet is far away from the coil, and the changing magnetic flux in the coil generates an induced current (Figure 1dii). The induced current in the coil reaches its maximum value when the distance between the magnet and the coil reaches its maximum value (Figure 1diii). Conversely, when the magnet approaches the coil, it generates an opposing induced current, resulting in the production of alternating current (Figure 1div). The open circuit voltage (V_{OC}^{EMG}) and short circuit current (I_{SC}^{EMG}) of the EMG can be expressed as follows:

$$V_{OC}^{EMG} = N\frac{d\Phi}{dt} \tag{7}$$

$$I_{SC}^{EMG} = \frac{V_{OC}^{EMG}}{R} \tag{8}$$

where V_{OC}^{EMG} is the open-circuit voltage of the EMG, N is the number of turns of the coil, $\frac{d\Phi}{dt}$ is the rate of change of the magnetic flux, I_{SC}^{EMG} is the short-circuit current of the EMG, and R is the resistance. To better demonstrate the magnetic field variation of the EMG, finite element analysis is also performed using COMSOL to simulate the magnetic flux distribution between the coil and the magnetic field, as depicted in Figure S3b (Supporting Information). The results of the simulation are in good agreement with the experimental results.

In summary, the vibration response of the MM-HNG is closely related to the mass of the attached magnet, the coil parameters, the vibration conditions, etc. These relationships are described in detail below.

2.2. Electrical Performance of the MM-HNG

2.2.1. Application Scenario and Structure Schematic of MM-HNG

Based on the above theoretical analysis, the effect of the number of turns of the coil in the stator on the output of the EMG is first investigated by using the shaker as a vibration source. According to the Equation:

$$N = \frac{\left[\pi\left(D_1 - D_2\right)\left(D_1 + D_2 + 2h\right)n\right]}{4h} \tag{9}$$
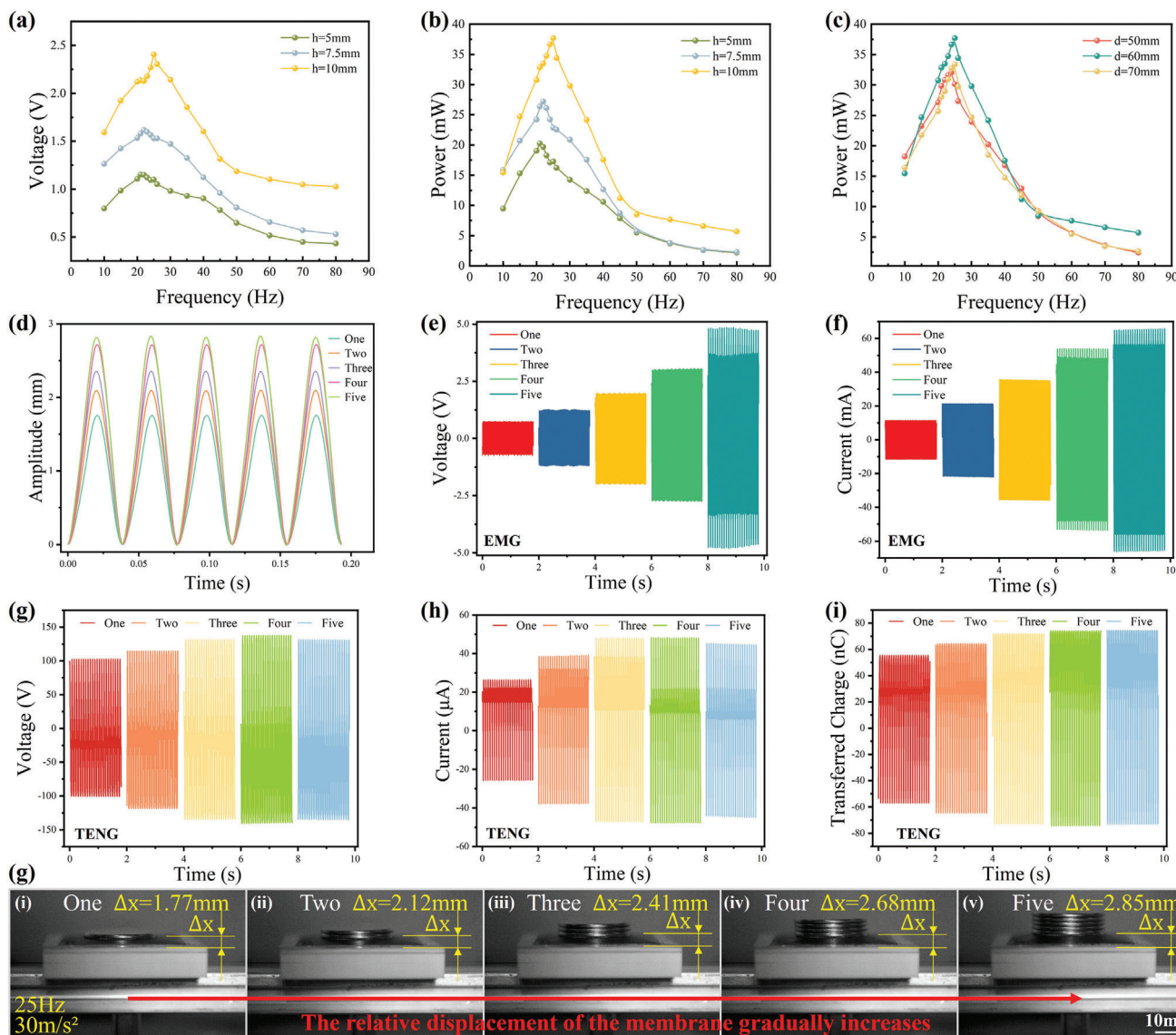
In Equation 9, N is the number of turns of the coil, D_1 is the outer diameter of the coil, D_2 is the inner diameter of the coil, h is the height of the coil, and n is the number of layers of the coil. Coils of different diameters and heights are selected to vary the number of turns and the effective magnetic inductance range for the experiment, as shown in **Figures 2a–c** and S4 (Supporting Information). The experimental results show that the output voltage increases continuously with the increase in the number of turns of the coil, and the output current decreases slightly. This phenomenon is attributed to the increased coil resistance and the decreased effective area for cutting the magnetic inductance due to the higher number of turns. Further, we calculate the output power by Equation:

$$P = VI \tag{10}$$

and finally found that the coil with a height of 10 mm and an outer diameter of 60 mm provides the best output, so this coil was chosen for the subsequent experimental investigations.

To further investigate the vibration conditions of MM-HNG, an experimental analysis is conducted on the number of additional magnets. The number of magnets is increased by adopting a same-pole outward approach. The results show that the number of additional magnets significantly affected the performance of the MM-HNG. In the experiment, the frequency and acceleration can be precisely adjusted by the signal generator. Figure 2d illustrates the variation in the amplitude of the MM-HNG with the number of additional magnets under the condition of 25 Hz, 30 m s⁻². Figure S5 (Supporting Information) shows in more detail the amplitude of the MM-HNG with different numbers of magnets under the acceleration of 10, 20, 30 m, and 40 m s⁻². It can be observed that with the increase in the number of additional magnets, the amplitude of the membrane can be effectively increased. This phenomenon can be well explained by Equations 3 and 4; as the additional mass m increases, it slightly alters the membrane's natural vibration frequency, thereby increasing the membrane's amplitude. Meanwhile, Figure 2e–i also shows the variation of electrical power at 25 Hz, 30 m s⁻² with different numbers of magnets. Specifically, Figure 2e,f shows the output of EMG; indicating that the output voltage and current increase with the number of magnets reaching 9.7 V and 62 mA with five additional magnets. This is because increasing the number of magnets enhances the strength of the magnetic field, which subsequently increases the amplitude of the membrane vibrations, thereby boosting the EMG power.

Figure 2g–i shows the output of TENG, it can be observed that the TENG output initially increases with the number of magnets but then levels off. With four additional magnets, the output voltage, current, and charge reach 275 V, 46 µA, and 132 nC, respectively. This is because as the number of magnets increases, the relative displacement of the membrane vibration increases, thereby enhancing the output of the TENG, as shown

ADVANCED
SCIENCE NEWS

www.advancedsciencenews.com

ADVANCED
MATERIALS
TECHNOLOGIES

www.advmattechnol.de

Figure 2. Different structural parameters on the electrical output of the MM-HNG. Variation of a) voltage and b) power with frequency for different coil heights. Variation of c) power with frequency for different coil diameters. d) Amplitude variation curves of FEP membranes with different numbers of additional magnets. e) Open-circuit voltage and f) short-circuit current of the EMG under the effect of different numbers of additional magnets. g) Open-circuit voltage, h) short-circuit current, and i) transferred charge of the TENG under the effect of different numbers of additional magnets. j) Displacement of MM-HNG with different numbers of additional magnets.

in Equation 1. However, as the mass of additional magnets continues to increase, the charge saturates, and the output levels off. To further explore how the mass of additional magnets affects the amplitude of the MM-HNG, the impact of varying numbers of additional magnets on the vibration of the MM-HNG at 25 Hz and 30 m s^{-2} is carefully observed using a high-speed camera, as shown in Figure 2j and Movie S1 (Supporting Information). The displacements with different numbers of additional magnets are clearly visible, as shown in Figure 2ji–v. It demonstrates that as the number of additional magnets increases from one to five, the amplitude increases from 1.77 to 2.85 mm. The maximum displacement reaches 2.85 mm when the mass of additional

magnets is five, which is in line with the experimental trend mentioned above.

2.2.2. Electrical Output of the MM-HNG Under Different Vibrations

Figure 3 provides a more detailed view of the electrical output of the MM-HNG with a different number of magnets at varying accelerations and frequencies. Figures 3a and S6 (Supporting Information) show the voltage, current, and transferred charge of the TENG output of the MM-HNG at different accelerations of 30 Hz. It can be seen that when the acceleration reaches a
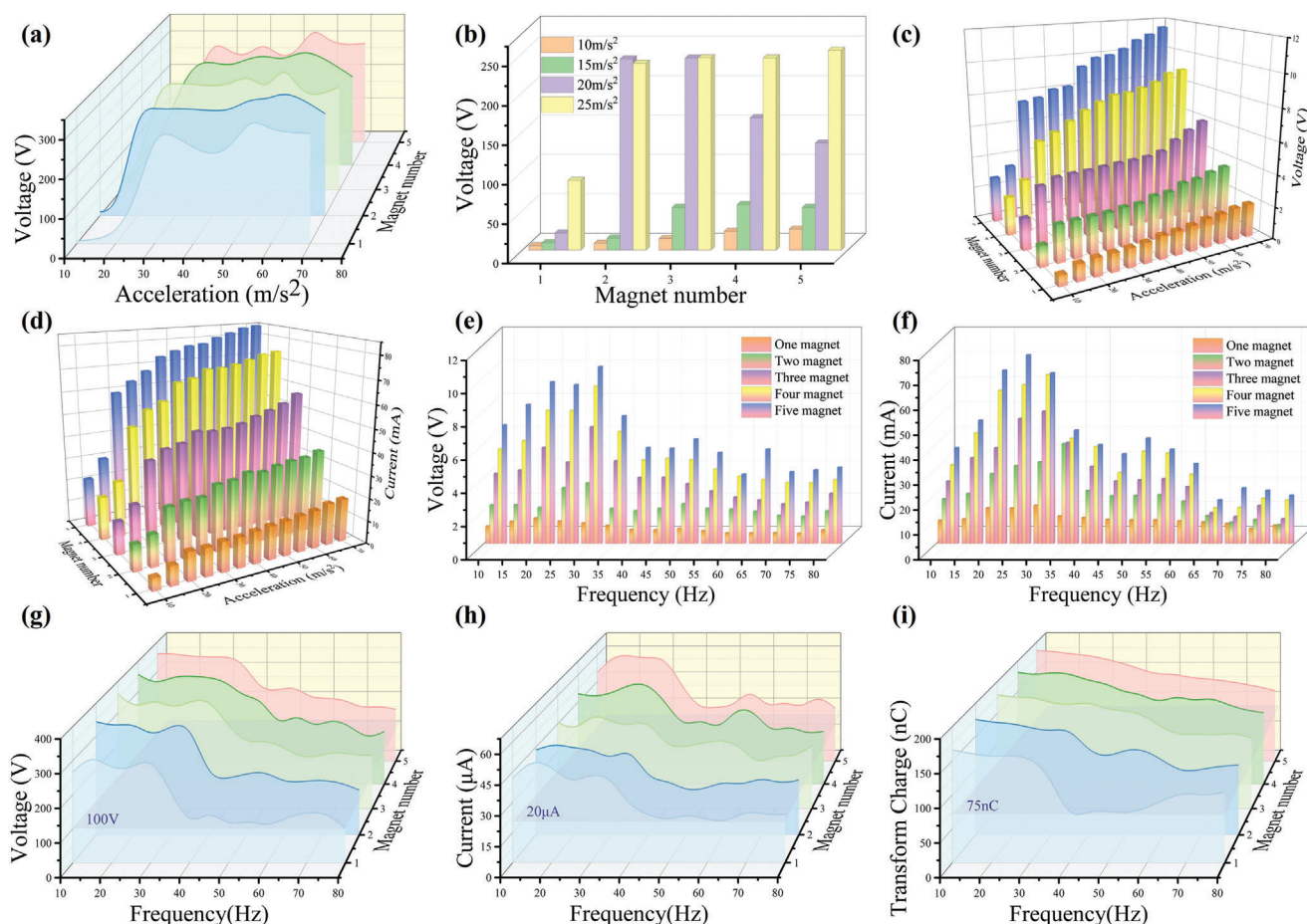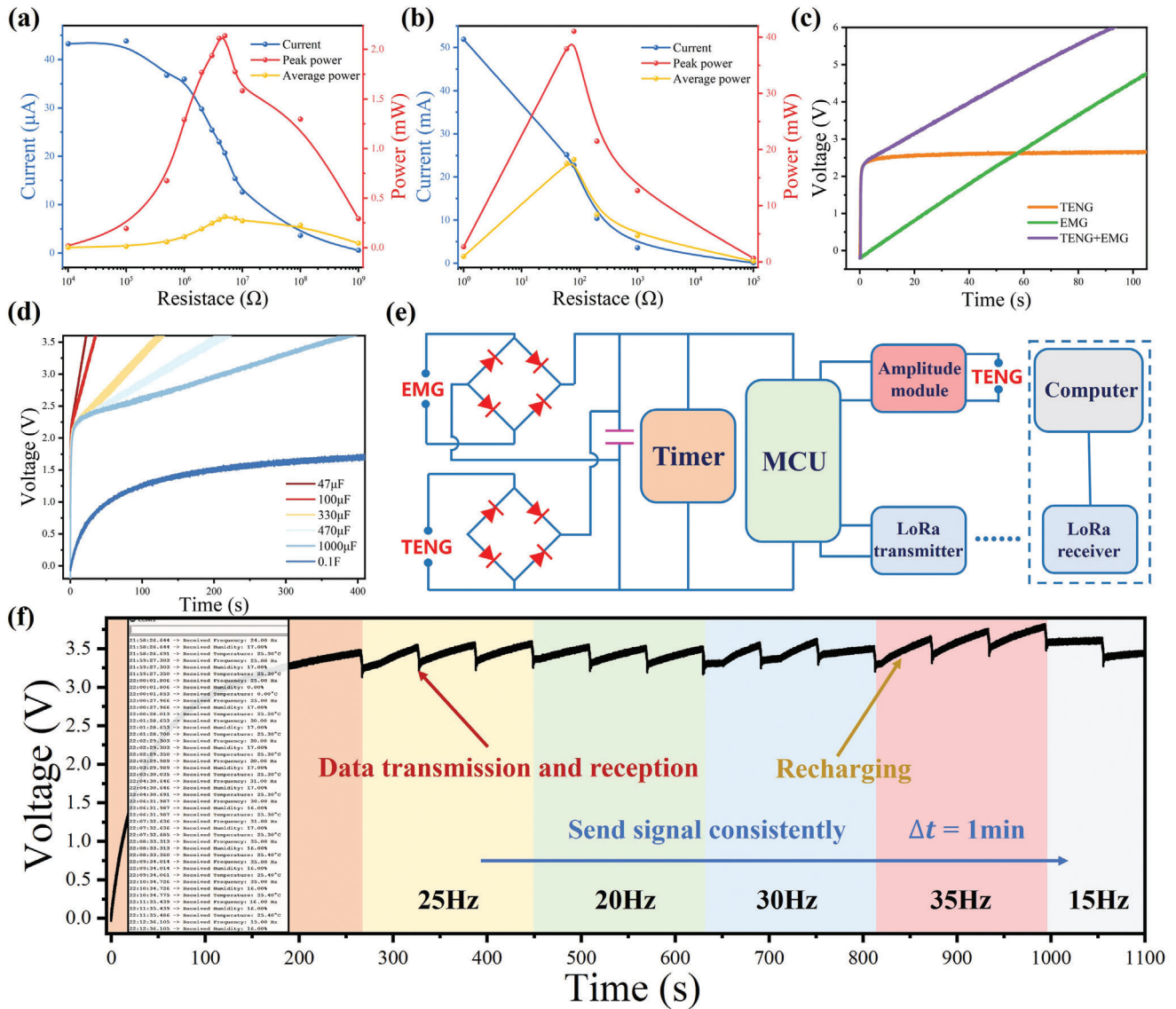
Figure 3. Output performance of the MM-HNG under various excitations. a) Voltage of TENG with different numbers of magnets under different accelerations. b) Voltage of TENG with different numbers of magnets under low acceleration. c) Voltage and d) current of EMG under various accelerations with different numbers of magnets. e) Voltage and f) current of EMG with different numbers of magnets at different frequencies. g) Voltage, h) current, and i) transferred charge output of TENG with different numbers of magnets under different accelerations.

certain level, the voltage output tends to stabilize and remain above 250 V, the current output tends to stabilize and remain above 40 mA, and the transferred charge tends to stabilize and remain above 120 nC. More specifically, Figure 3b illustrates that under low acceleration conditions, increasing the number of additional magnets will increase the amplitude of the MM-HNG, thereby improving output performance. However, it is important to note that additional magnets do not always correlate with enhanced performance. If the acceleration is insufficient, having too many magnets may prevent the MM-HNG from reaching its vibration state—meaning it cannot achieve the initial vibration state appropriate for that magnet configuration. This can ultimately reduce the amplitude of the MM-HNG and decrease the output of the TENG. Therefore, under low acceleration conditions, it is crucial to select the appropriate mass of additional magnets. Figure 3c,d illustrates the electrical output of the EMG of the MM-HNG at 30 Hz at various accelerations. It is observed that the output change is comparable to that of the TENG in that the output increases with acceleration. However, when the acceleration reaches a certain level, the rate of increase in output begins to slow down. Figure 3a–d also illustrates that the MM-HNG

can maintain a relatively excellent performance output for both TENG and EMG when the acceleration reaches a certain value ($\approx$20m s^{-2}).

Figure 3e,f displays the changes in EMG output across various frequencies, demonstrating a trend where the output initially increases and then decreases with rising frequencies. This behavior occurs because as the frequency increases, the system may not have sufficient displacement or amplitude to effectively respond to higher frequencies, resulting in a diminished output as the frequency continues to increase. Nonetheless, it's important to note that the maximum voltage reaches 11.3 V, the maximum current reaches 69.4 mA, the voltage output consistently exceeds 3 V, and the current output remains above 15 mA, both its maintained a good output. The output variation of TENG at different frequencies is shown in Figure 3g–i and the output variation is similar to that of EMG when the acceleration matches the frequency. The maximum voltage reaches 357 V, the maximum current reaches 58 μA, and the maximum transferred charge reaches 179 nC. At any frequency of 30 m s^{-2}, the output voltage is always higher than 100 V, the current is always higher than 20 μA, and the transferred charge is always higher than 75 nC. This

ADVANCED
SCIENCE NEWS

www.advancedsciencenews.com

ADVANCED
MATERIALS
TECHNOLOGIES

www.advmattechnol.de

Figure 4. A totally self-powered long-distance wireless sensing system based on the MM-HNG. The current, peak power, and average power of a) TENG and b) EMG vary with load resistance under the conditions of 30 Hz and 30 m s^{-2}. c) The comparison of the charging performance with separate TENG, separate EMG, and parallel connection of TENG and EMG for a capacitor (100 μF). d) Charging performance of capacitors with the MM-HNG from 47 μF to 0.1 F. e) Energy management strategy circuit diagram display of the MM-HNG totally self-powered long-distance wireless sensing system. f) Voltage waveforms are stored and regulated during operation.

demonstrates the MM-HNG's significant performance over the frequency range of 10–80 Hz. Such capability enables it to capture broadband vibration energy, making it versatile for use in various applications.

2.3. Output Power and Energy Management Strategy for the MM-HNG

Based on the results of previous studies, we conducted experiments and calculated the output power and average power of the MM-HNG, as shown in **Figure 4a,b**. These figures demonstrate the relationship between current, peak power, average power, and external load resistance for both the TENG and EMG of the MM-HNG at 30 Hz and 30 m s^{-2}, respectively. Peak power and average power are calculated by

$$P_{Max} = I^2 R \qquad (11)$$

$$P_{Average} = \frac{\int_0^T I^2 R dt}{T} \qquad (12)$$

At a load resistance of 5 MΩ, the peak power of TENG reaches 2.2 mW, and the average power is 0.26 mW, with a peak power density of 380.4 W m^{-3}. Conversely, at a load resistance of 80 Ω, the peak power of EMG reaches 41 mW, and the peak power density is 736 W m^{-3}. These results highlight the superior energy

**ADVANCED
SCIENCE NEWS**

www.advancedsciencenews.com

**ADVANCED
MATERIALS
TECHNOLOGIES**

www.advmattechnol.de

output of the MM-HNG. Figure 4c also shows that the charging efficiency of the storage capacitor is significantly improved when the TENG and EMG are operated simultaneously, which in turn enhances the signaling frequency of the subsequent self-powered monitoring system. Figure 4d depicts the synchronized operation of the TENG and EMG when charging capacitors with different capacitances (Figure S7, Supporting Information provides details of the charging circuit). The data confirm that the MM-HNG is capable of efficiently charging supercapacitors with a capacity of 0.1 F. These results underscore the excellent energy performance of the MM-HNG.

Therefore, we designed a totally self-powered long-distance wireless sensing system based on the MM-HNG. This system leverages the MM-HNG's excellent performance to supply power to the MCU, enabling long-distance monitoring of parameters such as frequency, temperature, and humidity. The circuit diagram of the self-powered wireless signal monitoring system is illustrated in Figure 4e. This system consists of an MM-HNG, a 0.1 F supercapacitor, a timer, an MCU module including a LoRa transmitter and charge amplifier, and a computerized LoRa receiver. The MM-HNG charges a 0.1F supercapacitor, which powers the MCU module via a timed on/off circuit. The MCU module recognizes and processes the information before the LoRa transmitter sends the wireless data. This setup allows for timed signal transmission and ensures the sustainability of the power supply. The computer at the receiving end receives the wireless data through the LoRa, capable of transmitting up to 1 kilometer per minute and counting. Comprehensive monitoring data is presented in Figure 4f, showing the voltage at both ends of the energy storage capacitor and the continuous operation of the system under different and continuous vibration frequencies. This also provides a clear picture of how the voltage changes and how the system switches between sleep and wake modes.

When operating at an acceleration of 30 m s^{-2}, the MM-HNG with four additional magnets is selected for the experiment by choosing a moderate mass and adapting to a wider range of frequencies versus contrasting charging speeds (Figure S8, Supporting Information). If the capacitor is charged above 3.3 V, the system is activated, and data is transmitted once every minute using the sleep function of the timer. The data is displayed on the frequency screen in a scrolling manner. Additionally, the system can regulate the frequency of the vibrator and is capable of fast charging capacitors at an acceleration of 30 m s^{-2} and a frequency of 15–35 Hz. Therefore, MM-HNG can be used to collect vibration energy from mechanical equipment under different vibration conditions to meet the energy consumption requirements for data transmission in various working conditions. In addition, Figure S9 (Supporting Information) shows that the MM-HNG operates stably at 30 Hz and transmits signals once per minute, demonstrating its ability to maintain operation for extended periods. The energy consumed for a single emission can be calculated by Equation 13:

$$E = \frac{1}{2} CV^2 \tag{13}$$

The system requires ≈0.54 J to punch a 0.1F capacitor from 0 to 3.5 V and uses ≈0.005 J to emit a single signal. The average power of EMG in MM-HNG is 22 mW and the average power of TENG

is 0.26 mW, which can ensure that the capacitor is made to have enough power during the system's sleep time to allow the system to send a signal every minute to satisfy the continuous sending of the signal. In addition, the timing of each signal transmission can be adjusted by modifying the resistance of the external timer, ensuring automatic wireless transmission of sensor signals. This highlights the potential of the MM-HNG self-powered wireless signal monitoring system for applications in distributed sensor nodes and unattended equipment monitoring.
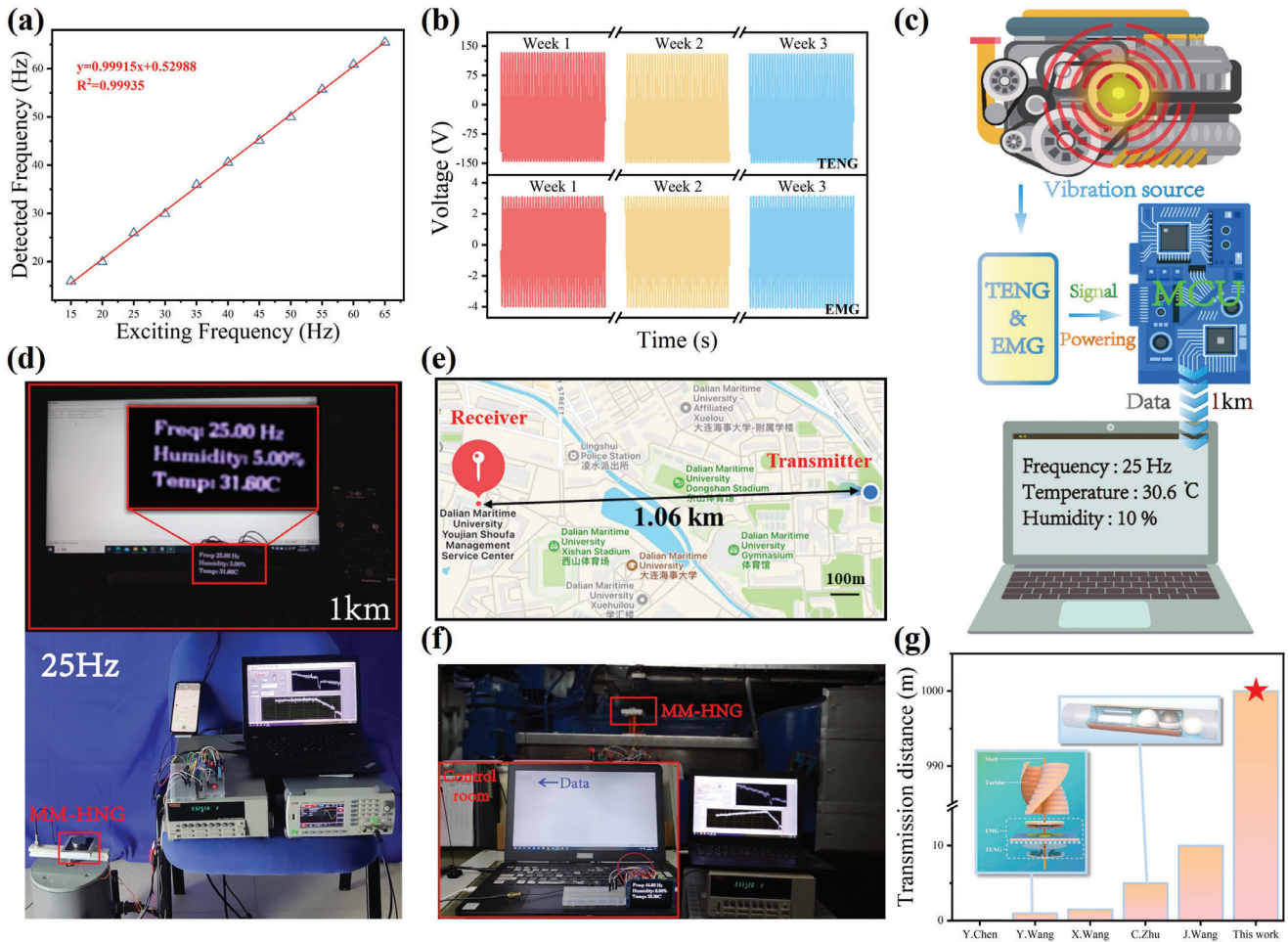
2.4. Demonstration of the MM-HNG

In addition to the vibration energy harvest, the TENG of the MM-HNG is also capable of being used as a sensor for measuring frequency due to the TENG's pronounced and responsive electrical signal. **Figure 5a** shows the frequency detection function of TENG in the MM-HNG, comparing the experimental frequency with the actual frequency using FFT analysis. As a result, the MM-HNG can accurately detect the vibration frequency of the equipment. Additionally, the TENG and EMG components inside the MM-HNG are tested for durability under 30 Hz and 30 m s^{-2} acceleration conditions(the experiment is conducted in three weeks, 20 min for each experiment), and SEM tests are performed on the FEP film before and after use, the results of which are shown on Figures 5b and S10 (Supporting Information). The results show that the MM-HNG can maintain continuous and stable operation in complex environments. Repeatability experiments are conducted on MM-HNG, as shown in Figure S11 (Supporting Information), the performance of MM-HNG did not change much under repeated experiments, which also proved the feasibility of MM-HNG.

The realization of distributed wireless sensor networks requires a large number of wireless sensor nodes, and the power supply method and sensing distance of the sensor nodes affect the continuity and coverage of the wireless sensor network. Therefore, we have continued the practical application of the totally self-powered wireless energy monitoring system based on the MM-HNG for equipment vibration energy harvest. Figure 5c illustrates the process of vibration energy harvesting and the implementation of self-powered environmental monitoring by the MM-HNG in a realistic scenario. Under the excitation of the vibration source, the electrical energy output from the TENG and EMG is stored in a capacitor, which supplies power to the MCU. The temperature, humidity, and vibration signals (detected by the TENG) are transmitted to the MCU module, which analyzes and processes them and drives the LoRa to transmit the various signals to the computer cloud for real-time monitoring. In addition, the wide frequency characteristics of the MM-HNG enable it to work on various mechanical devices (the frequencies and accelerations of various devices are shown in Table S1, Supporting Information).

To better explore the signal transmission distance of the totally self-powered long-distance wireless sensor system based on the MM-HNG. Figure 5d,e, and Supplementary Movie S2 (Supporting Information) demonstrate that the data transmission can still be achieved with a separation of 1 km between the signal transmitting end and the signal receiving end. In this experiment, the fixed acceleration is 30 m s^{-2} and the frequencies are 25, 20, 30,

**ADVANCED
SCIENCE NEWS**

www.advancedsciencenews.com

**ADVANCED
MATERIALS
TECHNOLOGIES**

www.advmattechnol.de

Figure 5. Demonstration of the MM-HNG. a) Accuracy of TENG used for frequency monitoring. b) Durability experiments of TENG and EMG in the MM-HNG. c) Flowchart of a totally self-powered long-distance wireless sensing system. d) Long-distance wireless transmission diagram of the MM-HNG in a campus environment. e) Actual transmission distance. f) Environmental monitoring diagram of the MM-HNG in a real cabin environment. g) Comparison Chart for Transmission Distance.

35, and 15 Hz with amplitudes of 1.2, 1.9, 0.8, 0.6, and 3.3 mm, respectively. It proves that the MM-HNG self-powered wireless signal monitoring system can achieve long-distance signal transmission, which is an excellent solution to the problem of limited distance of wireless signal transmission equipment. Therefore, the MM-HNG's totally self-powered long-distance wireless sensing system can achieve long-distance signal transmission and monitoring. Furthermore, the system is tested on a real ship's engine with the computer receiver placed in the central control room, approximately two compartments away from the engine room. It can be seen that the central control room can receive the vibration frequency of the engine as well as the temperature and humidity in real-time (the frequency of the marine engine is ≈45 Hz, acceleration is ≈73.5m s^{-2} and amplitude is ≈0.9 mm), as shown in Figure 5f and Movie S3 (Supporting Information). Figure S12 (Supporting Information) shows the voltage waves of the wireless transmission signals from the MM-HNG self-powered wireless monitoring system during the operation of a marine diesel engine, transmitting data once per minute and is capable of continuous operation. Figure 5g also compares

the transmission distance of this system with existing hybrid generation-based systems[26,31,45–47] and finds that the transmission distance of this system is much greater than other systems. This provides an effective solution to the problems of sensor energy supply and the limited range of wireless signal transmission devices, laying a solid foundation for the construction of an intelligent wireless sensor network.

3. Conclusion

In summary, a novel high-performance magnetic mass-enhanced triboelectric-electromagnetic hybrid nanogenerator (MM-HNG) is proposed for vibration energy harvesting. The MM-HNG can efficiently harvest broadband vibration energy and achieve accurate frequency sensing over a wide frequency range. At 30 Hz, the maximum power of TENG in MM-HNG reaches 2.14 mW with a peak power density of 380.4 W m^{-3}, while the highest power of EMG reaches 41.04 mW with a peak power density of 736 W m^{-3}, which can quickly charge a 0.1 F supercapacitor. In addition, a totally self-powered long-distance

**ADVANCED
SCIENCE NEWS**

www.advancedsciencenews.com

**ADVANCED
MATERIALS
TECHNOLOGIES**

www.advmattechnol.de

wireless sensing system is constructed, which consists of an MM-HNG, a 0.1 F supercapacitor, a timer, an MCU module including a LoRa transmitter and charge amplifier, and a computerized LoRa receiver. The supercapacitor charged by the MM-HNG powers the microcontroller unit (MCU), which can be automatically woken up by an external timer. The acquired information, including the temperature, humidity, and vibration frequency of the equipment, can be wirelessly transmitted every minute for long distances. Finally, the transmission range of the MM-HNG self-powered wireless signal monitoring system is verified, and the wireless transmission range can reach up to 1 km. The MM-HNG self-powered wireless signal monitoring system is also demonstrated on a real ship. In the actual ship demonstration, the temperature, humidity, and frequency information of the actual generator engine equipment is successfully monitored in the control room. This work provides an effective solution for fully self-powered long-distance wireless sensing and demonstrates that the MM-HNG has a wide range of application scenarios in IoT fields, such as smart machines, smart transportation, and smart factories.

4. Experimental Section

Fabrication of the MM-HNG: The MM-HNG consisted of a TENG and EMG. TENG consisted of FEP (30 µm in thickness) brushed with conductive ink, conductive fabric, and copper wires, the edges of the FEP film were not brushed with conductive ink, which was to avoid short-circuiting between electrodes, and the copper wires were glued as the signal wires to the ink and the conductive fabric, respectively, and the dimensions of the FEP film and the conductive fabric were 50×50 mm. The EMG consisted of a coil, which was 60 mm in diameter, 10 mm in thickness, turn count of 2750 turns, and coil resistance of 80Ω; and a magnet, which was 35 mm in diameter and 2 mm in thickness. It was fixed to the FEP film with insulating double-sided tape, which also served to increase the amplitude of the FEP film. The support structure was made of PLA material by 3D printing technology to fix the TENG and EMG, and the size of the support structure was $70 \times 70 \times 10$ mm. In the totally self-powered long-distance wireless sensing system, the temperature and humidity sensor module is DHT11, which operates with a voltage of 3.3–5 V, a humidity measurement range of 20–95%, and a temperature measurement range of 0 to 50 °C.

Vibration Status Monitoring of the MM-HNG: The MM-HNG was fixed on a shaker (JZK-50), and the vibration signal was generated by a signal generator (UTG2062B), amplified by a signal amplifier (YE5874A) to drive the shaker to generate vibration. A high-speed camera (PHANTOM V2012: 20–28 VDC INPUT-10 AMP MAX@24VDC) and PCC 4.0 software were used to observe the vibration status of the MM-HNG, and the actual amplitude and acceleration of the MM-HNG were obtained by a laser displacement sensor (HG-C1050) and an acceleration sensor (DAQ280G).

Electrical Output Measurements: An electrostatic meter (Keithley 6514) was used to measure the electrical signals of the MM-HNG including open-circuit voltage, short-circuit current, and transferred charge. The electrical signals were then sent to a computer through a DAQ unit (NI-9215) to be observed and stored using Labview software for observation and storage. Arduino Nano was chosen to process the sensor signals and transmit the information wirelessly through the LoRa module.

Supporting Information

Supporting Information is available from the Wiley Online Library or from the author.

Conflict of Interest

The authors declare no conflict of interest.

Data Availability Statement

The data that support the findings of this study are available from the corresponding author upon reasonable request.

[1] N. Saeed, H. Malik, A. Naeem, U. Bashir, *Multimedia Tools Appl.* **2024**, *83*, 20699.

[2] A. B. Guiloufi, S. El khediri, N. Nasri, A. Kachouri, *Multimedia Tools Appl.* **2023**, *82*, 42239.

[3] S. Aslam, M. P. Michaelides, H. Herodotou, *IEEE Internet Things J.* **2020**, *7*, 9714.

[4] T. Kalsoom, N. Ramzan, S. Ahmed, M. Ur-Rehman, *Sensors* **2020**, *20*, 6783.

[5] H. Liazid, M. Lehsaini, A. Liazid, *J. Network Comput. Appl.* **2023**, *211*, 103556.

[6] A. Alaerjan, *Sensors* **2023**, *23*, 975.

[7] R. Dogra, S. Rani, H. Babbar, D. Krah, M. A. Khan, *Wireless Commun. Mobile Comput.* **2022**, *2022*, 8006751.

[8] X. Li, Y. Cao, X. Yu, Y. Xu, Y. Yang, S. Liu, T. Cheng, Z. L. Wang, *Appl. Energy* **2022**, 306.

[9] Y. Wang, X. Liu, Y. Wang, H. Wang, H. Wang, S. L. Zhang, T. Zhao, M. Xu, Z. L. Wang, *ACS Nano* **2021**, *15*, 15700.

[10] Q. Zhang, Z. Xi, Y. Wang, L. Liu, H. Yu, H. Wang, M. Xu, *Front. Mater.* **2022**, *9*, 896953.

[11] C. Chang, X. He, Z. Han, L. Pei, Z. Wang, Y. Ji, *Sustainable Energy Fuels* **2022**, *6*, 693.

[12] T. Du, F. Dong, Z. Xi, M. Zhu, Y. Zou, P. Sun, M. Xu, *Small* **2023**, *19*, 2300401.

[13] J. Yu, J. Yao, D. Li, J. Yu, H. Xiao, H. Zhang, J. Shang, J. Wu, Y. Liu, R.-W. Li, *Appl. Phys. Lett.* **2023**, *123*, 043901.

[14] S. Veeralingam, O. P. Nanda, S. Badhulika, *J. Alloys Compd.* **2023**, *961*, 171127.

[15] H. Yu, Z. Xi, Y. Zhang, R. Xu, C. Zhao, Y. Wang, X. Guo, Y. Huang, J. Mi, Y. Lin, T. Du, M. Xu, *Nano Energy* **2023**, *107*, 108182.

[16] F.-R. Fan, Z.-Q. Tian, Z. Lin Wang, *Nano Energy* **2012**, *1*, 328.

**ADVANCED
SCIENCE NEWS**

www.advancedsciencenews.com

**ADVANCED
MATERIALS
TECHNOLOGIES**

www.advmattechnol.de

[17] J. Wang, W. Ding, L. Pan, C. Wu, H. Yu, L. Yang, R. Liao, Z. L. Wang, *ACS Nano* **2018**, *12*, 3954.

[18] X. Wang, C. Zhu, M. Wu, J. Zhang, P. Chen, H. Chen, C. Jia, X. Liang, M. Xu, *Sens. Actuators, A* **2022**, *344*, 113727.

[19] J. Liu, P. Xu, J. Zheng, X. Liu, X. Wang, S. Wang, T. Guan, G. Xie, M. Xu, *Nano Energy* **2022**, *101*, 107633.

[20] M. Chahari, E. Salman, M. Stanacevic, R. Willing, S. Towfighian, *Smart Mater. Struct.* **2024**, *33*, 055034.

[21] M. Mousavi, M. Alzgool, B. Davaji, S. Towfighian, *Small* **2023**, *20*, 2304591.

[22] K. Barri, Q. Zhang, I. Swink, Y. Aucie, K. Holmberg, R. Sauber, D. T. Altman, B. C. Cheng, Z. L. Wang, A. H. Alavi, *Adv. Funct. Mater.* **2022**, *32*, 2203533.

[23] Z. Guan, L. Liu, X. Xu, A. Liu, H. Wu, J. Li, W. Ou-Yang, *Nano Energy* **2022**, *104*, 107879.

[24] X. Zhang, J. Zhao, X. Fu, Y. Lin, Y. Qi, H. Zhou, C. Zhang, *Nano Energy* **2022**, *98*, 107209.

[25] T. Quan, Y. Wu, Y. Yang, *Nano Res.* **2015**, *8*, 3272.

[26] S. M. Purushothaman, M. F. Tronco, B. Kottathodi, I. Royaud, M. Ponçot, N. Kalarikkal, S. Thomas, D. Rouxel, *Polymer* **2023**, *283*, 126179.

[27] C. Ye, D. Liu, P. Chen, L. N. Y. Cao, X. Li, T. Jiang, Z. L. Wang, *Adv. Mater.* **2023**, *35*, 2209713.

[28] F. R. Fan, W. Tang, Y. Yao, J. Luo, C. Zhang, Z. L. Wang, *Nanotechnology* **2014**, *25*, 135402.

[29] Y. Wang, Z. Qian, C. Zhao, Y. Wang, K. Jiang, J. Wang, Z. Meng, F. Li, C. Zhu, P. Chen, H. Wang, M. Xu, *Adv. Mater. Technol.* **2022**, *8*, 2201245.

[30] X. Li, Q. Gao, Y. Cao, Y. Yang, S. Liu, Z. L. Wang, T. Cheng, *Appl. Energy* **2022**, *307*, 118311.

[31] J. Zhao, J. Mu, H. Cui, W. He, L. Zhang, J. He, X. Gao, Z. Li, X. Hou, X. Chou, *Adv. Mater. Technol.* **2021**, *6*, 2001022.

[32] P. Lu, H. Pang, J. Ren, Y. Feng, J. An, X. Liang, T. Jiang, Z. L. Wang, *Adv. Mater. Technol.* **2021**, *6*, 2100496.

[33] C. Han, Z. Cao, Z. Yuan, Z. Zhang, X. Huo, L. Zhang, Z. Wu, Z. L. Wang, *Adv. Funct. Mater.* **2022**, *32*, 220511.

[34] C. Zhu, M. Wu, C. Liu, C. Xiang, R. Xu, H. Yang, Z. Wang, Z. Wang, P. Xu, F. Xing, H. Wang, M. Xu, *Adv. Energy Mater.* **2023**, *13*, 2301665.

[35] Y. Pang, Y. Fang, J. Su, H. Wang, Y. Tan, C. Cao, *Adv. Mater. Technol.* **2023**, *8*, 2201246.

[36] W. Xie, L. Gao, L. Wu, X. Chen, F. Wang, D. Tong, J. Zhang, J. Lan, X. He, X. Mu, Y. Yang, *Research* **2021**, *2021*, 5963293.

[37] M. Toyabur Rahman, S. M. Sohel Rana, M. Salauddin, P. Maharjan, T. Bhatta, H. Kim, H. Cho, J. Y. Park, *Appl. Energy* **2020**, *279*, 115799.

[38] C. Wu, S. Yang, G. Wen, C. Fan, *Rev. Sci. Instrum.* **2021**, *92*, 055003.

[39] J. He, X. Fan, D. Zhao, M. Cui, B. Han, X. Hou, X. Chou, *Sci. China Inf. Sci.* **2021**, *65*, 142401.

[40] I. Kim, D. Kim, *ACS Appl. Mater. Interfaces* **2022**, *14*, 34081.

[41] X. Gao, M. Huang, G. Zou, X. Li, Y. Wang, *Nano Energy* **2023**, *111*, 108356.

[42] S. Gao, S. Feng, J. Wang, H. Wu, Y. Chen, J. Zhang, Y. Li, R. Wang, X. Luo, H. Wei, X. Zeng, *ACS Appl. Mater. Interfaces* **2023**, *15*, 34764.

[43] J. Shen, Y. Yang, Z. Yang, B. Li, L. Ji, J. Cheng, *Nano Energy* **2023**, *116*, 108818.

[44] P. Maharjan, S. Lee, T. Bhatta, G. B. Pradhan, K. Shrestha, S. Jeong, S. M. S. Rana, J. Y. Park, *Adv. Mater. Technol.* **2022**, *8*, 2201545.

[45] X. Wang, S. Wang, Y. Yang, Z. L. Wang, *ACS Nano* **2015**, *9*, 4553.

[46] Y. Chen, Y. Jie, J. Zhu, Q. Lu, Y. Cheng, X. Cao, Z. L. Wang, *Nano Res.* **2021**, *15*, 2069.

[47] J. Wang, X. Chen, S. Xie, G. Bao, F. Wu, C. Meng, *ACS Appl. Mater. Interfaces* **2023**, *15*, 53476.